CZECH TECHNICAL UNIVERSITY IN PRAGUE

Faculty of Nuclear Sciences and Physical Engineering

Department of Physics

Research project

Study of the properties of charm and beauty quarks with non-photonic electrons

Bc. Jan Vaněk

Supervisor: Mgr. Jaroslav Bielčík, Ph.D.

Prague, 2016

ČESKÉ VYSOKÉ UČENÍ TECHNICKÉ V PRAZE
FAKULTA JADERNÁ A FYZIKÁLNĚ INŽENÝRSKÁ
PRAHA 1 - STARÉ MĚSTO, BŘEHOVÁ 7 - PSČ 115 19

Katedra: fyziky **Akademický rok:** 2015/2016

VÝZKUMNÝ ÚKOL

Posluchač: Bc. Jan Vaněk

Obor: Experimentální jaderná a částicová fyzika

Vedoucí úkolu: Mgr. Jaroslav Bielčík, Ph.D., FJFI ČVUT

Název úkolu (česky/anglicky):

Studium vlastností půvabných a krásných kvarků pomocí nefotonických elektronů

Study of the properties of charm and beauty quarks with non-photonic electrons

Pokyny pro vypracování:

1. Fyzika těžkých vůní v experimentu STAR
2. Detektor STAR
3. Analýza experimentálních údajů
4. Optimalizace výběrových kritérii na selekci elektronů pomocí HFT
5. Korekce na geometrickou akceptanci detektoru a účinnost rekonstrukce elektronů
6. Spektrum nefotonických elektronů
7. Diskuze a závěr

Výzkumný úkol bude vypracován v anglickém jazyce.
Součástí zadání výzkumného úkolu je jeho uložení na webové stránky katedry fyziky.

Literatura:

[1] Ramona Vogt, Ultrarelativistic Heavy-Ion Collisions, Elsevier 2007.

[2] Mustafa Mustafa, Experimental study of electrons from heavy flavor hadrons decays in Au+Au collisions at 200, 62.4 and 39 GeV in the STAR experiment at RHIC, Ph.D. Thesis, Purdue University 2013.

[3] ALICE Collaboration, Measurement of beauty-hadron decay electrons in Pb–Pb collisions at 2.76 TeV with ALICE, J.Phys.Conf.Ser. 612 (2015) 1, 012037.

[4] ALICE Collaboration, Measurement of electrons from beauty hadron decays in pp collisions at 7 TeV, Phys.Lett. B721 (2013) 13.

Datum zadání: 23.10.2015 .....

Datum odevzdání: 24.06.2016 ***vedoucí katedry***

Prohlášení:

Prohlašuji, že jsem svou bakalářskou práci vypracoval samostatně a použil jsem pouze podklady (literaturu, software, atd.) uvedené v přiloženém seznamu.

Nemám závažný důvod proti užití tohoto školního díla ve smyslu 60 Zákona .121/2000 Sb., o právu autorském, o právech souvisejících s právem autorským a o změně některých zákonů (autorský zákon).

V Praze dne 22. 06. 2016 Jan Vaněk

Title:
Study of the properties of charm and bottom quarks with non-photonic electrons

Author: Bc. Jan Vaněk

Specialization: Experimental nuclear physics

Sort of project: Research project

Supervisor: Mgr. Jaroslav Bielčík, Ph.D.

Abstract: A hot and dense state of matter, the quark-gluon plasma, in which the quarks and gluons are no longer trapped inside colorless hadrons, is created in ultra-relativistic heavy-ion collisions. Large colliders, such as the Large Hadron Collider in CERN laboratory and the Relativistic Heavy-Ion Collider in Brookhaven National Laboratory, are used for study of the heavy-ion collisions. Large detectors are placed at these colliders in order to measure particles created in the heavy-ion collisions. One of interesting particle species created and studied are the open heavy-flavor mesons: D mesons containing c quark and B mesons containing b quark. These quarks are created predominantly in initial phase of the heavy-ion collision, during the hard scattering, before the quark-gluon plasma ignition. They therefore can be used as a probe of the quark-gluon plasma. The open heavy-flavor mesons have too short lifetime to be detected directly. The only way is to measure their decay products. One of used possibilities are non-photonic electros which originate in semi-leptonic decay of the open-heavy flavor mesons. An introduction to analysis of the non-photonic electros in Au+Au collisions at $\sqrt{s_{NN}} = 200$ *GeV measured by STAR experiment at Relativistic Heavy-Ion Collider in the year 2014 is provided in this thesis.*

Key words: Heavy-ion collisions, non-photonic electrons, open-heavy flavor mesons, quark-gluon plasma, Relativistic Heavy-Ion Collider, STAR experiment

Acknowledgement

I would like to thank Mgr. Jaroslav Bielčík, Ph.D. for patient guidance and all the useful advice. I would also like to thank my family and friends for their support.

Contents

List of Figures

List of Tables

Introduction

Strongly interacting particles, the quarks and gluons, are trapped inside colorless hadrons in contemporary Universe. This property of strong iteraction is referred as confinement. Non-perturbative space-time Lattice QCD (Quantum Chromo-Dynamics) calculations predict cross-over phase transition from confined hadronic matter to phase called the Quark-Gluon Plasma (QGP), which occurs at temperature approx. 170 MeV and baryon chemical potential $\mu_B \to 0$ [1]. In this phase (the QGP) the quarks and gluons are no longer bound inside hadrons. It is believed that the QGP was present in the Universe about 10^{-5} s after the Big Bang [2].

The QGP is experimentally studied via ultra-relativistic heavy-ion collisions. Large synchrotron accelerators and colliders are used for accelerating and colliding heavy ions, where two most powerful and well known are the Relativistic Heavy Ion Collider (RHIC) in Brookhaven National Laboratory, Long Island, USA and the Large Hadron Collider (LHC) in CERN laboratory near Geneva, Switzerland. Experiments dedicated predominantly to study of the QGP and heavy-ion collisions are located at both of these colliders. At the LHC it is ALICE (A Large Ion Collider Experiment) and at the RHIC it is STAR (Solenoidal Tracker At RHIC) and PHENIX (Pioneering Hight Energy Nuclear Interaction eXperiment) experiments.

Signatures of the QGP in heavy-ion collisions at STAR and other experiments are based on comparison of heavy-ion data with proton-proton data, where it is assumed that no QGP is present. There are three main effects observed in heavy-ions collisions, which are considered to be evidence of presence of the QGP. The first one is quarkonium production suppression in heavy-ion collision, the second one is asymmetry in transverse momentum p_T spectrum called flow, and the third signature is high p_T particles suppression, which is also referred as jet-quenching.

All these phenomenons can be measured either for all particles produced in the collision, or it is possible to focus on specific particle species. For example, it is interesting to study open heavy-flavor mesons, i.e. D mesons, containing c quark and B mesons, containing b quark, as they both are good probe to the QGP. Due to large masses of c and b quarks, they are produced predominantly in initial phase of the heavy-ion collision, during the hard scattering, before ignition of the QGP fireball. Therefore they have to pass thorough the fireball, where they interact with the surrounding medium, and so they carry information

about the QGP.

Unfortunately the D and B mesons have very short lifetime and can not be detected directly. The only option to measure their decay products. Two most used decay channels of the open heavy-flavor mesons are the hadronic channel and the semi-leptonic channel. This channel has advantage that electrons are relatively easy to detect and collider experiments at RHIC and LHC have means to distinguish them from other charged particles, mainly pions, kaons and protons. In case of the STAR experiment it is the Time Of Flight (TOF) system and Barrel Electro-Magnetic Calorimeter (BEMC). Another benefit of this channel is that only one decay product is reconstructed, in contrast with hadronic channel, where all decay products have to be reconstructed. The main disadvantages of the semi-leptonic channel are that it does not provide sufficient information about p_T and kinematics of mother particle and that there is a large photonic electrons background.

There are two main methods, how to measure the NPE. The firs one is to reconstruct the photonic background and then subtract it from the inclusive electron spectrum. The second one is direct detection of the NPE based on measurement of the Distance Of Closest Approach to the primary vertex (designated DCA or d_0), which is the closest distance between the primary vertex and the reconstructed electron track in plane transverse to the collider beam axis. The main disadvantage of the DCA method is that it requires very good spatial resolution of the detector. The main advantage of this method is that it is able to directly distinguish NPE from D and B mesons, which is not possible with background subtraction method.

Predominantly the DCA method of NPE measurement in heavy-ion collisions is discussed in this thesis. The first chapter is dedicated to physical motivation for heavy-ion collisions, general properties of the heavy-ion collisions and signatures of the QGP in heavy-ion collisions. The second chapter is about the RHIC and its accelerator chain and about STAR detector and its subdetectors. The third chapter summarises general properties of NPE and NPE measurements performed by STAR, PHENIX and ALICE experiments. The fourth chapter is about NPE analysis of Run14 (year 2014) Au+Au collisions at $\sqrt{s_{NN}} = 200$ GeV measured by STAR and in the fifth chapter a discussion and conclusion is provided.

Chapter 1

Heavy-ion collisions

Ultra-relativistic heavy-ion collisions are one of the main experimental tools for measurement of extreme state of matter known as the quark-gluon plasma (QGP). In this chapter there are three sections. The first is about physical motivation for the heavy-ion collisions, the second is about properties of the heavy-ion collisions and the third provides summary of experimental signatures of the QGP in heavy-ion collisions.

1.1 Physical motivation

Heavy-ion collisions are used for study of the nuclear matter. Despite its name, the nuclear matter does not describe atomic nuclei, but infinite volume of protons and neutrons with finite ratio between them. This concept is used in theory of strong interaction, the quantum chromo-dynamics (QCD), for performing theoretical calculations.

One of the goals of the QCD is to obtain phase diagram of the nuclear matter. Example of schematic phase diagram can be seen in Fig. 1.1, where the calculations were performed using non-perturbatice space-time Lattice-QCD. On the y axis there is temperature T and on the x axis there is baryon-chemical potential μ_B. The shaded area represents anticipated first order transition, the dashed line at low μ_B is cross-over transition which at $\mu_B \to 0$ occurs at critical temperature $T_{crit} \approx 170\,\mathrm{MeV}$ [1] and E is critical point. Point M marks state of nuclear matter present inside atomic nuclei and the remaining points represent place of chemical freeze-out (see Section 1.2.2) from statistical model.

There are three phases of nuclear matter plotted in Fig. 1.1. The first one is hadronic phase at lower T and μ_B, in which quarks and gluons are trapped inside colorless hadrons. This state of nuclear matter arises from property of strong interaction called confinement and it is dominant in contemporary Universe. The second one is color super-conductor, which appears at low T and high μ_B (i.e. at high hadronic density). Protons and neutrons are fermions and in hadronic phase they have to obey Fermi statistics but in this phase they combine

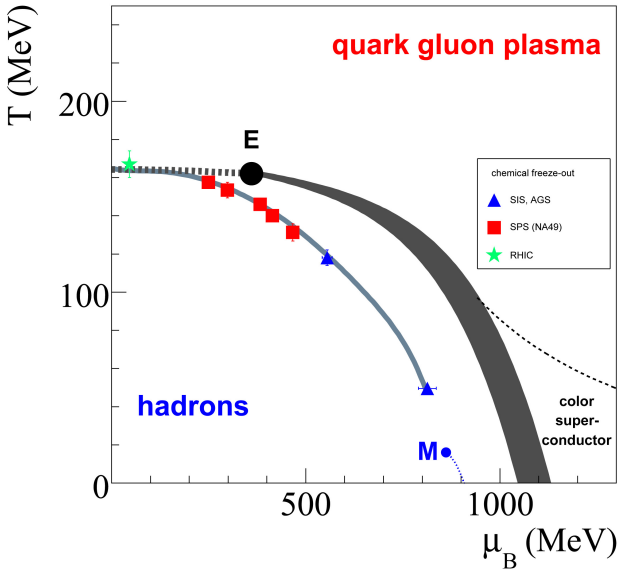

Fig. 1.1: Phase diagram of nuclear matter. On the y axis there is temperature T and on the x axis there is baryon-chemical potential μ_B. The shaded area represents anticipated first order transition, the dashed line at low μ_B is cross-over transition and E is critical point. Point M marks state of nucl. matter present inside atomic nuclei and the remaining points represent place of chemical freeze-out (see Section 1.2.2) from statistical model. Individual phases of nuclear matter are denoted in the plot. Taken from Ref. [1].

into so-called Cooper pairs, which follow Bose-Einstein statistics so the whole system can "fall" to lower energetic state. This mechanism is very similar to the one observed in metallic super-conductors, where the Cooper pairs are formed by electrons.

The last phase is the QGP, which is the most important in context of heavy-ion collisions. In the QGP the quarks and gluons are no longer confined inside hadrons, hence this phase is also referred as deconfinement. Quarks and gluons inside the QGP are not completely free as they interact via strong interaction but their freedom is much bigger than in hadronic phase. It is believed that the QGP was present in very early stage of the Universe, to be more specific approx. 10^{-5} s after the Big Bang [2], so study of heavy-ion collisions, in which the QGP is produced, also provides information about history of the Universe.

The main accelerators with heavy-ion program are the Large Hadron Collider (LHC) in CERN Laboratory near Geneva, Switzerland and the Relativistic Heavy Ion Collider (RHIC) in Brookhaven National Laboratory, USA. When they operate at their top energy of collisions, they both explore the part of the phase diagram, where $\mu_B \to 0$, so all transitions observed in such collisions are

cross-overs which occur at $T_{crit} \approx 170\,\mathrm{MeV}$ [1]. RHIC has advantage, compared to LHC, that it is able to collide particles at variety of energies so it can scan the phase diagram in mode detail. Example of such measurement is a successful attempt to prove existence of the critical point by STAR experiment in Ref. [3].

To conclude, the main goals of study heavy-ion collisions is to determine properties of the QGP and the transitions between the QGP and normal (confined) hadronic matter. So far it is experimentally proven that at low μ_B and temperature $T_{crit} \approx 170\,\mathrm{MeV}$ the transition is cross-over [1] and that the critical point exists [3]. Other properties of the phase diagram, such as exact position of the critical point, are sill to be determined.

1.2 General characteristics of heavy-ion collisions

1.2.1 Geometry

Heavy ions used for in accelerators are relatively large objects and it is not possible to neglect their size. Signal from each individual collision of two nuclei is strongly dependent on initial geometry. One of the main geometry characteristics is centrality which is basically distance between centres of the two nuclei in plane perpendicular to their movement. This distance is denoted the impact parameter b and is shown in Fig. 1.2. If $b \approx 0$ the collision is called central, if $b \to 2R$, where R is radius of the colliding nuclei, then it is called peripheral.

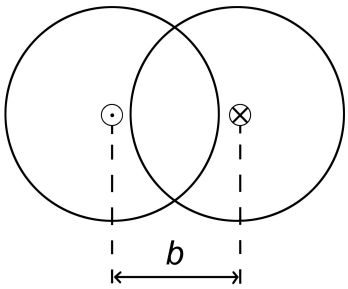

Fig. 1.2: Scheme of heavy-ion collision in plane perpendicular to the movement of the nuclei. The distance between the centres of the projectiles is called impact parameter b.

The impact parameter can not be measured directly and for that reason is not much used. Instead, the centrality can be parameterised by number of participants N_{part}, which is number of nucleons from both colliding nuclei that participated in given collision. The remaining nucleons are called spectators, which keep on going after the collision. Therefore the spectators can be detected by so called zero-degree calorimeters placed in the beam axis and they can be subsequently used for centrality determination.

It is also convenient to define system of coordinates. By convention it is right-handed Cartesian system where the z axis is parallel to the beam axis, the x axis is horizontal and y axis is vertical, as shown in Fig. 1.3. Azimuthal angle ϕ is measured in x-y plane from the x axis (also shown in Fig. 1.3), longitudinal angle θ is measured form the z axis, but is is not used very often. Pseudorapidity η defined as

$$\eta = -\ln\left[\tan\left(\frac{\theta}{2}\right)\right] \tag{1.1}$$

is usually used instead.

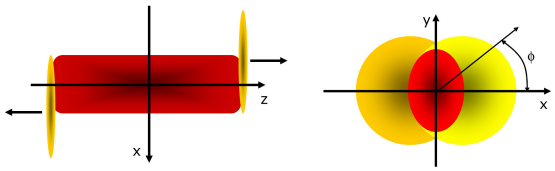

Fig. 1.3: System of coordinates in heavy-ion collision. The z axis is parallel to the beam axis, the x axis is horizontal and y axis is vertical. Taken from Ref. [4].

1.2.2 Space-time evolution

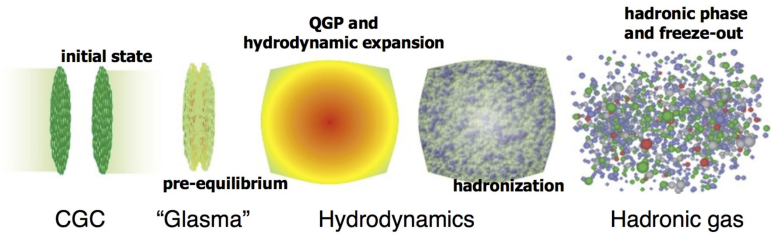

Fig. 1.4: Diagram of time evolution of heavy-ion collision, where z is the beam axis, t is time, T_c is critical temperature (above denoted T_{crit}), T_{ch} is temperature of chemical freeze-out and T_{fo} is temperature of kinetic freeze-out. For more detailed description see the text. Taken from Ref. [1].

The heavy-ion collision can be divided into several phases, which are shown in Fig. 1.5. In initial state the nuclei are far apart and they do not interact with each other. Theoretical description of the initial state is still not completely resolved but one of the most used models today is the color-glass condensate (CGC). The colliding nuclei are travelling at ultra-relativistic speed, hence they

are relativistically contracted and they appear as discs in the laboratory system. The CGC describes these discs as fragile walls made (predominantly) of gluons.

The primary interaction of the nucleons of the two colliding nuclei is called the hard scattering and it is the phase of the heavy-ion collision where particles with high p_T are created. Very shortly after the hard scattering, probably less than 1 fm/c [5], a fireball of QGP is ignited. The fireball expands following relativistic viscous hydrodynamics, until its temperature falls down to critical temperature T_{crit}. At this point deconfinement can not be present any more and the fireball hadronizes.

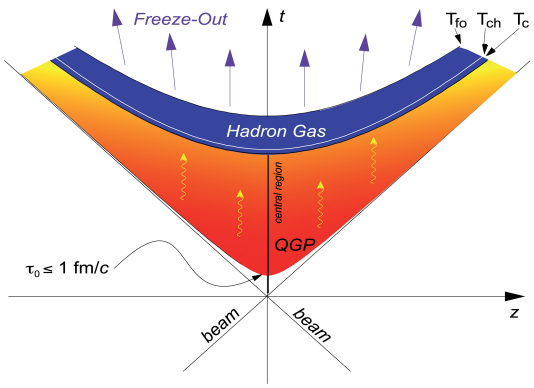

Fig. 1.5: Individual pases of heavy-ion collision in $z-t$ plane, where t is time and z is the beam axis. For more detailed description see the text. Taken from Ref. [5].

The hadronization process is a complex event with multiple stages, as shown in Fig. 1.4. After cooling down under critical temperature T_{crit}, there is a mixture of strongly interacting hadrons whose species can change. The volume is further increasing and the temperature dropping down to temperature of chemical freeze-out T_{ch}, under which the hadrons are interacting with each other, but the composition remains unchanged. T_{ch} is very likely close to T_{crit}. As the volume increases even more, the temperature drops below temperature of kinetic freeze-out T_{fo}, under which the hadrons do not interact with each other and the composition remains unchanged.

1.3 Experimental signatures of the QGP

There are several signals proving existence of the QGP in heavy-ion collisions. In this section examples of most important signals are presented. They are particle production suppression in heavy-ion collisions compared to proton-proton collisions, elliptic flow and higher order harmonics and finally so called jet quenching.

1.3.1 Particle production suppression

Particle production suppression in heavy-ion collisions is quantified by nuclear modification factor R_{AA} defined as [12]

$$R_{AA}(p_T) = \frac{\mathrm{d}N_{ch}^{AA}(p_T)/\mathrm{d}p_T}{\langle N_{coll}\rangle \mathrm{d}N_{ch}^{pp}(p_T)/\mathrm{d}p_T}, \tag{1.2}$$

where N_{ch}^{AA} is number of charged particles created in given heavy-ion collision, N_{ch}^{pp} is number of charged particles created in given proton-proton collision and $\langle N_{coll}\rangle$ is mean number of binary (parton-parton) collisions in heavy-ion collision. This variable is defined so that if heavy-ion collision were simple superposition of individual binary collisions, the R_{AA} would be equal to unity. In other words, $R_{AA} = 1$ means, that there is either no QGP created in studied collision or other effects in given collision are much stronger than the QGP effects.

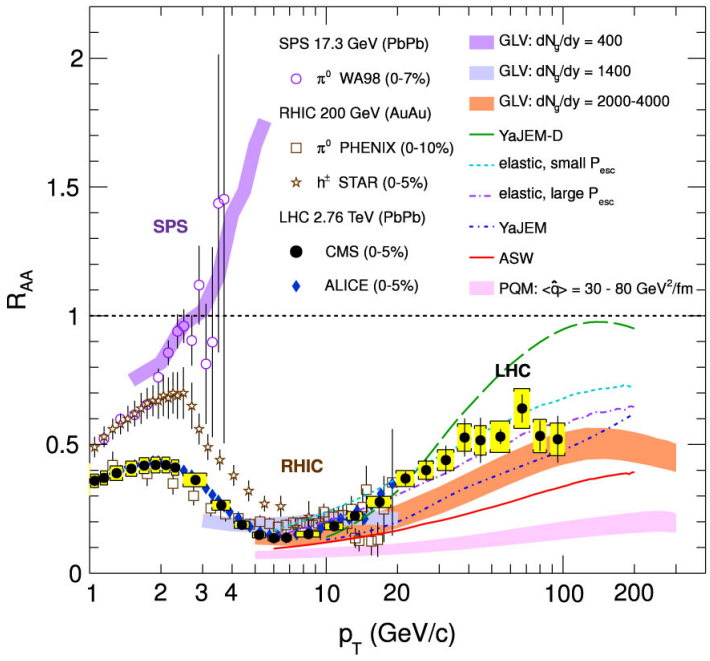

Fig. 1.6: Nuclear modification factor R_{AA} as function of p_T. Shown are data from multiple experiments at RHIC (BNL), SPS and LHC (CERN). Comparison with multiple models is also plotted. Taken from Ref. [6].

Experimental results show that R_{AA} is below unity for all p_T at LHC and RHIC. Example of such measurement is in Fig. 1.6, where the data come from multiple experiments at RHIC (BNL), SPS and LHC (CERN). Comparison with

multiple models is also plotted[1]. This result means that particle production is suppressed in heavy-ion collisions compared to proton-proton collisions, which suggests existence of the QGP at LHC and RHIC.

Particles created in hard scattering in initial state of the heavy-ion collision have to travel through subsequently ignited QGP fireball, where they loose energy and momentum. As a result they can stopped completely, which means they will not be detected. As it turned out, the primary mechanism of particle production in heavy-ion collisions is hadronization described in Section 1.2.2 and not the hard scattering.

1.3.2 Elliptic flow and higher harmonics

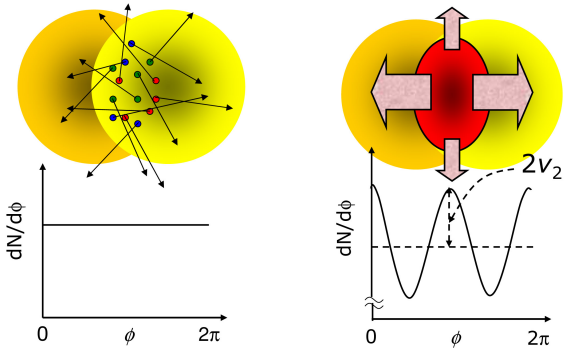

Fig. 1.7: Scheme for demonstration of elliptic flow v_2. On the left is situation when mean free path of particles inside the fireball is larger than the size of the fireball - no elliptic flow is present. On the right is situation when the mean free path of the particles is smaller than the fireball - elliptic flow is present. Taken from Ref. [4].

Elliptic flow v_2 and higher order harmonics v_n are asymmetries in p_T azimuthal spectrum of given collision which arise from spatial asymmetry of overlap region of the colliding nuclei. As shown in Fig. 1.7 on the right, the fireball is smaller in direction parallel to the event plane than in direction perpendicular to the event plane. This means that particles in the event plane will obtain higher p_T than the particles out of it, due to higher pressure gradient in the event plane. As the spatial asymmetry can be approximated by an ellipse, the resulting p_T asymmetry will be also elliptical and for that reason is called elliptic flow. The elliptic flow was observed in heavy-ion collisions, which also suggests that the mean free path of the particles inside the fireball is smaller than size of the fireball itself.

[1]GLV = Gyulassy-Levai-Vitev, YaJEM = Yet another Jet Energy-Loss Model, ASW = Armesto-Salgado-Wiedemann, PQM = Parton Quenching Model.

$$\frac{\mathrm{d}N}{\mathrm{d}\varphi} \propto 1 + 2\sum_{n=1}^{\infty} v_n \cos[n(\varphi - \Psi_n)] \tag{1.3}$$

Individual harmonic flows v_n ca be mathematically defined as coefficients of the particle azimuthal distribution Fourier series (1.3) as defined in Ref. [7]. The φ is here the azimuthal angle and the Ψ_n is the n-th order event plane.

Example of measurement of elliptic flow v_2 is shown in Fig. 1.8. The v_2 is here plotted as a function of p_T for several particle species in two centrality bins. The data is also compared to VISHNU model (Viscous Israel-Steward Hydrodynamics 'n' UrQMD). This plot shows that the expansion of the QGP fireball si well described by relativistic hydrodynamics.

Higher order harmonics arise from more complicated spatial asymmetries than ellipse, such as triangle - triangular flow v_3, etc. The highest order measured to this date was v_6 by ATLAS experiment at LHC. As shown in Ref. [8] higher order harmonics are less significant for higher n for semi-central and peripheral collisions, in central collisions the triangular flow v_3 exceeds the elliptic flow v_2, which is caused by nearly circular overlap of the colliding nuclei where higher order spatial asymmetries can be more significant than the elliptic one.

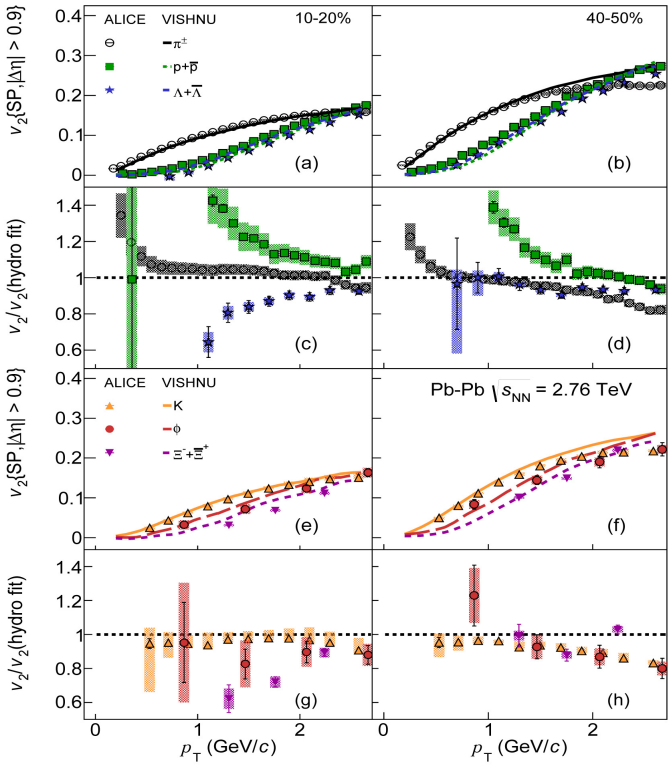

Fig. 1.8: (a), (b), (c), (d): Elliptic flow v_2 as a function of p_T measured by ALICE in Pb+Pb collisions at $\sqrt{s_{NN}} = 2.76$ TeV for multiple particle species and for two centrality bins. VISHNU model is also plotted. (c), (d), (g), (h): Ratio of experimental data and model. Taken from Ref. [9].

1.3.3 Jet quenching

Collimated, high energy showers of particles are observed in proton-proton and heavy-ion collisions and are called jets. They arise from hadronization of high-energetic partons originating in hard scattering. In proton-proton collisions there is nothing to influence the movement of the daughter partons and therefore the resulting jets can be fully reconstructed. In case of the heavy-ion collision one, or both daughter partons have to travel through the QGP where they loose energy as schematically shown in Fig. 1.9.

As a result one of the jets is suppressed compared to the other. The jet with higher energy (or p_T) is called leading or near-side jet and the one with lower energy is subleading or away-side jet. In case the hard scattering occurs close to the edge of the QGP fireball, one of the partons exits the fireball immediately and the other has to go through the whole volume. In this case the away-side jet can be suppressed completely, as shown in panel (b) in Fig. 1.10 for Au+Au

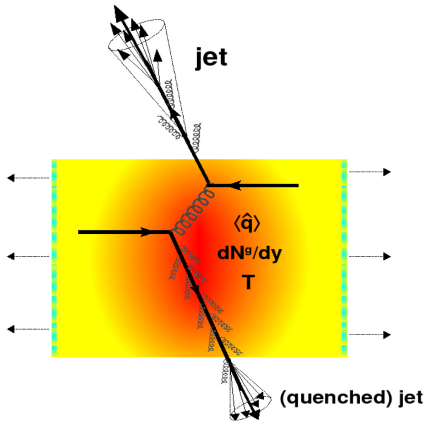

Fig. 1.9: Scheme for demonstration of jet quenching. Taken from Ref. [10]

collision. The same plot also shows that for d+Au collisions, no jet quenching is observed, i.e. in d+Au no QGP is created.

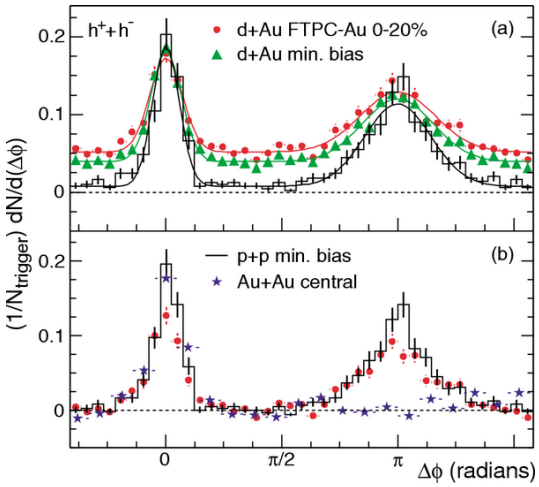

Fig. 1.10: Two-particle azimuthal distribution measured by STAR for d+Au and Au+Au collisions, both at $\sqrt{s_{NN}} = 200\,\mathrm{GeV}$. The leading, trigger particle was required to have $4 < p_T(trig) < 6\,\mathrm{GeV}/c$ and only associated particles with $2\,\mathrm{GeV}/c < p_T < p_T(trig)$ were chosen. Taken from Ref. [11].

Chapter 2

STAR experiment

2.1 The Relativistic Heavy-Ion Collider

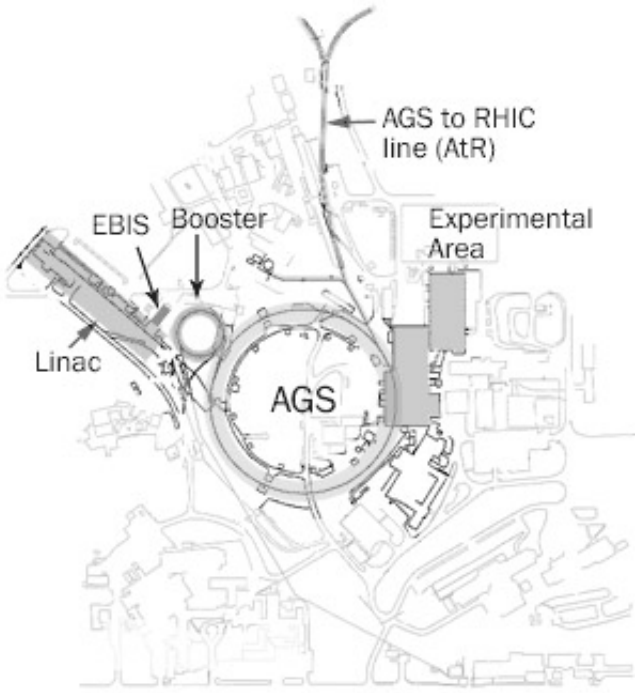

Fig. 2.1: RHIC accelerator chain used for heavy ions and protons. Taken from Ref. [13].

The Relativistic Heavy-Ion Collider is located in Brookhaven National Laboratory (BNL), Long Island, USA. It consists of two concentric synchrotrons

with circumference of 3,833.845 m [13], which are able to accelerate either protons or atomic nuclei. The most commonly used were protons and gold nuclei, but also copper, uranium or deuterium ions were used. The maximal energy of collisions is $\sqrt{s} = 500$ GeV for proton-proton system and $\sqrt{s_{NN}} = 200$ GeV (energy per nucleon pair) for Au+Au system.

The particles to be collided have to be preaccelerated before they enter the RHIC. The RHIC preacceleration complex is schematically shown in Fig. 2.1. The ^{197}Au ions are created in Electron Beam Ion Source (EBIS), in which they are preaccelerated to energy of 2 MeV [15]. After exiting the EBIS, the ions are stripped to Au^{32+} and are moved into Booster Synchrotron. Here six bunches are formed and the ions are accelerated to 95 MeV. Then they are stripped again to Au^{77+} when transferred to the AGS (Alternating Gradient Synchrotron). The AGS is filled by 24 bunches from Booster (i.e. from four Booster cycles), which are then regrouped into four bunches and the ions are further accelerated up to 8.86 GeV. After that the ions are fully stripped to Au^{79+} and injected into the RHIC, where 56 bunches per ring is stored (i.e. 112 bunches in RHIC).

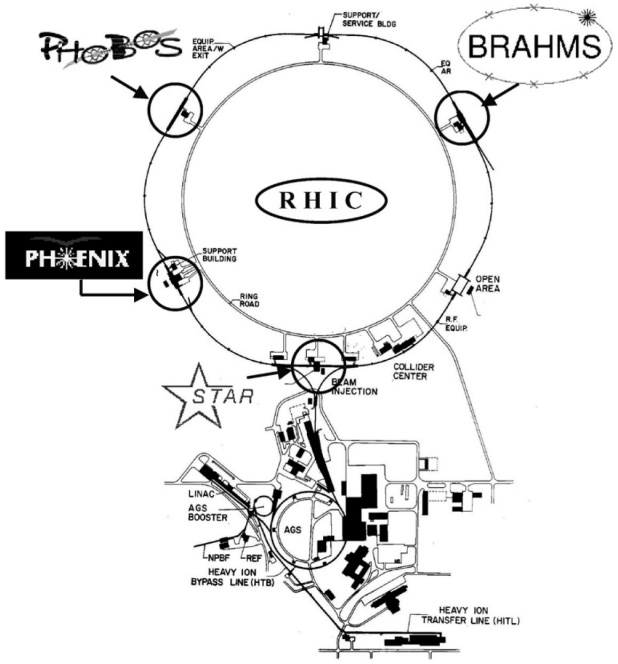

Fig. 2.2: Scheme of RHIC accelerator chain. Position of individual experiments at RHIC is highlighted. Taken from Ref. [14].

After the ions are accelerated to given energy between 8.86 GeV and 100 GeV per beam, the actual collisions can begin. There are six intersection regions along the RHIC, where collisions are possible. Experiments are located at four of those crossing points, as shown in Fig. 2.2. They are STAR (Solenoidal

Tracker At RHIC), PHENIX (Pioneering High Energy Nuclear Interaction eXperiment), PHOBOS and BRAHMS (Broad RAnge Hadron Magnetic Spectrometers). Only STAR and PHENIX are sill taking data, as PHOBOS and BRAHMS finished data taking in the year 2006.

2.2 STAR detector

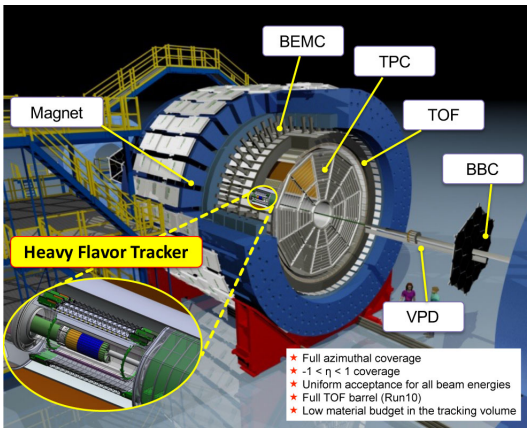

Fig. 2.3: STAR detector and its subdetectors. Taken from Ref. [16].

STAR experiment is designated primarily for study of the heavy-ion collisions and it si experiment, where the QGP was officially discovered. Description of the STAR detector is provided in this section. Schematic picture of the STAR detector is in Fig. 2.3.

It is a large solenoidal magnet that provides magnetic field of 0.5 T [17]. The field causes the charged particles to travel at curved trajectory, which allows to determine their momentum. STAR detector acceptance is 2π in azimuthal direction and $|\eta| < 1$ in longitudinal direction. A variety of subdetectors is located inside the magnet, where each one is used either for particle identification (PID) or for determining their energy and momentum. Important subdetectors are described below.

2.2.1 Heavy Flavor Tracker

The innermost detector is the Heavy Flavor Tracker (HFT), which replaced the Silicon Vertex Tracker (SVT) in the year 2014. It is a 4-layer silicon detector designated for primary and secondary vertex reconstruction. Its total acceptance is 2π in azimuthal direction and $|\eta| < 1.2$ in longitudinal direction. Its scheme is shown in Fig. 2.4. First two layers, closest to the beam axis, are silicon pixel (PXL) detectors, the third layer is Intermediate Silicon Tracker (IST)

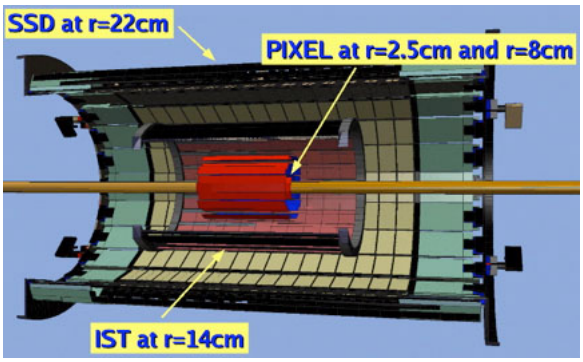

Fig. 2.4: Scheme of the HFT and its layers. Taken from Ref. [18].

and the fourth, outer layer is the Silicon Strip Detector (SSD). All information and values in this section are reproduced from Ref. [18] if not stated otherwise.

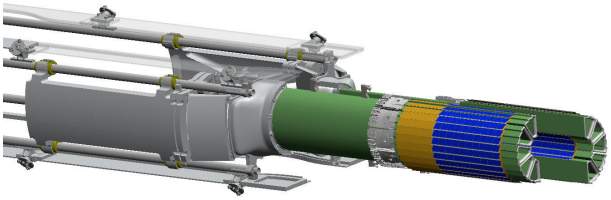

Fig. 2.5: Schematic view of STAR pixel detector and its support structure as innermost part of the HFT. Taken from ref. [18].

The STAR PXL detector is schematically shown in Fig. 2.5. It consists of 40 ladders, where 10 are in inner layer (2.5 cm from beam axis) and 30 are in outer layer (8.0 cm from beam axis). Each ladder carries 10 CMOS (Complementary Meta-Oxide Semiconductor) sensors with active area approximately 2 cm x 2 cm each. There are around 1,000 x 1,000 square 20.7 μm pixels at each sensor. The ladders are supported by 10 carbon composite beams, where one beam carries 3 outer and 1 inner ladder. As a result the PXL has hit resolution of 10 μm.

The third layer of the HFT is the IST, which consist of 144 sensors placed at 24 carbon-fibre ladders in distance of 14 cm from the beam axis. The schematic picture if the IST is sown in Fig. 2.6. Its main purpose is to increase track reconstruction precision by providing track points between the PXL and the TPC (Time Projection Chamber).

The fourth, outer, layer of the HFT is the SSD. It is the only part of the HFT, which was also part of the older SVT. The sensors remained unchanged but the readout system had to be upgraded due to insufficient readout frequency. The SSD consists of 20 ladders, each carrying 16 two-sided wafers in distance of 22 cm from the beam axis. The purpose of the SSD is basically the same

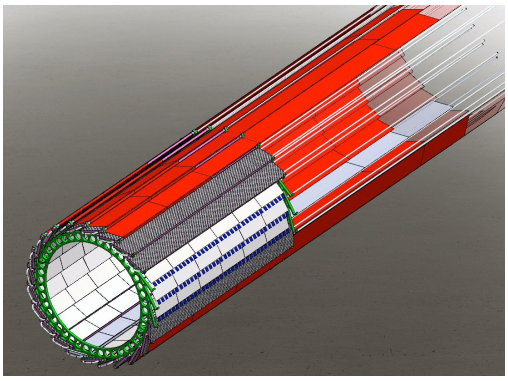

Fig. 2.6: Schematic view of STAR IST (Intermediate Silicon Tracker). Taken from Ref. [18].

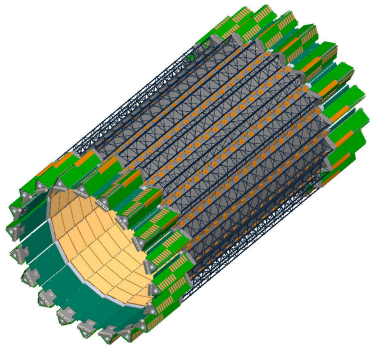

Fig. 2.7: Schematic view of STAR SSD (Silicon Strip Detector). Taken from Ref. [18].

as of the IST. It provides track points between the PXL and the TPC, which increases the track reconstruction accuracy.

Generally the HFT provides very good DCA (Distance Of Closes Approach, see Section 3.1) resolution of $\sim 30\,\mu$m at $p_T > 1.5\,\text{GeV}/c$ [16], which allows, for example, direct measurement of open-heavy flavor mesons, the D and B, as they have different lifetimes.

Basic principle of operation is the same for all HFT layers. Individual pixels or strips are silicon diodes connected in reverse direction. Sensitive part of the diodes is then depleted region of the PN junction. A passing charged particle creates electron-hole pairs in the depleted region. The electrons and holes are moved by electric field to opposite ends of the diode, where they are collected. Signal from electrons is used for analysis, as electron drift velocity in the semiconductor is higher than that of the holes.

2.2.2 Time Projection Chamber

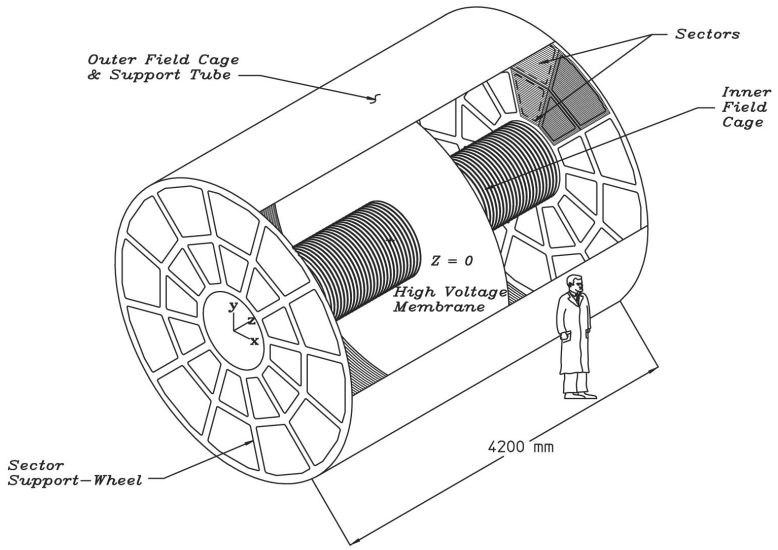

Fig. 2.8: Schematic view of STAR TPC (Time Projection Chamber). Taken from Ref. [19].

The Time Projection Chamber (TPC) is the main STAR detector used for particle identification and for determining particle momentum. It is a large cylinder (length 4.2 m, outer diameter 4.0 m, inner diameter 1.0 m) filled with mixture of methane and argon in ratio 10/90 at atmospheric pressure with 2 mbar overpressure. It has full (2π) coverage in azimuthal direction and $|\eta| < 1$ in longitudinal direction. As can be seen in Fig. 2.8 the volume of the TPC is divided in halves by High Voltage Membrane, which serves as cathode. At both ends of the TPC there are readout sectors which serve as an anode. There is inner and outer field cage placed on the wall of the TPC, which provides uniform electric field between the cathode and the readout sectors.

These sectors are MWPC (Multi-Wire Proportional Counters). A cutaway view of one of these pads can be seen in Fig. 2.9. When a charged particle travels through TPC volume, it creates electron-ion pairs by ionising argon atoms. The electrons are subsequently carried towards the readout pads by the electric field of 140 $\mathrm{V\,cm^{-1}}$, where they are detected. The MWPC detects the electrons by accelerating them in strong electric field applied to the anode grid and creating electron avalanches. The charge from the avalanches is subsequently collected by readout pads placed under the anode grid. The organic component of the TPC filling gas (methane) absorbs UV photons emitted by accelerated electrons

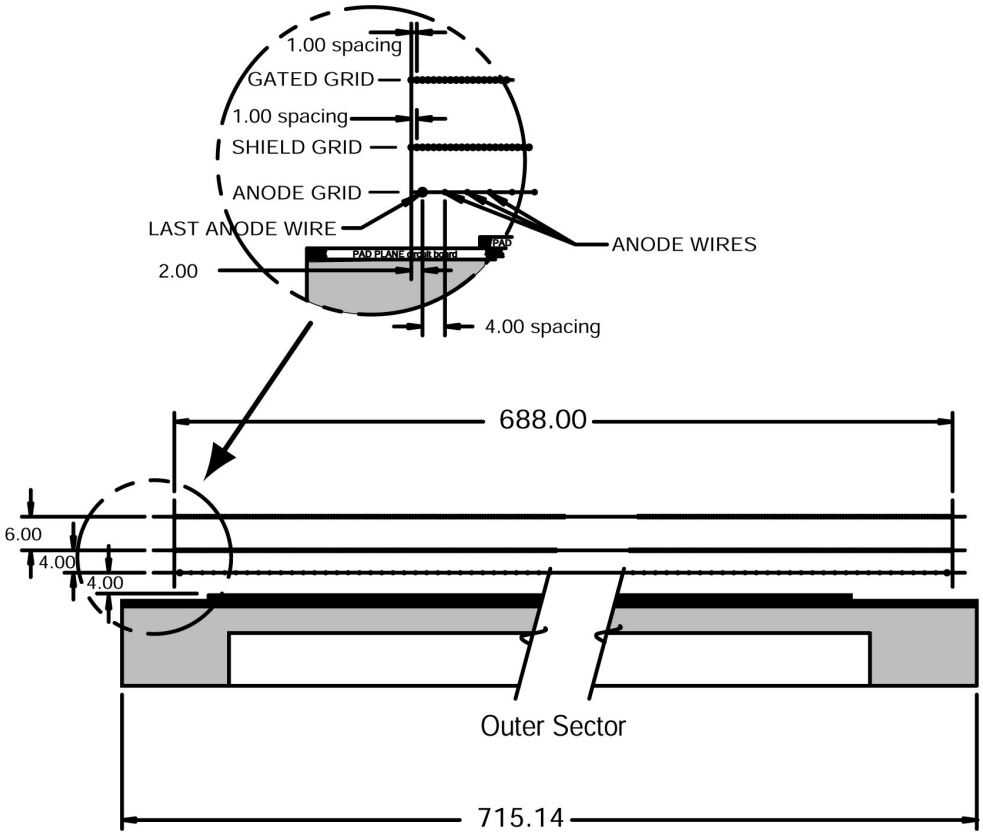

Fig. 2.9: Scheme of TPC outer sector MWPC pad. All dimensions are in millimeters. Taken from Ref. [19].

from the avalanches, which prevents creation of secondary avalanches by the UV photons. This precaution is necessary for particle identification by the TPC.

The particle identification in the TPC is based on information about particle energy-loss in the gas. The gas ionisation energy is assumed to be well defined, so the number of created electrons in one track is proportional to particle energy loss. The MWPC preserves information about number of detected electrons as amplification of signal is the same for all detected electrons. Thus the energy loss of given particle is proportional to charge collected by the readout pads. The (transverse) momentum of the particle is determined from radius of the track in the 0.5 T magnetic field of the STAR solenoid.

The TPC is the most important subdetector in STAR detector, as it is the the main particle identification and p_T determination tool in STAR. There is no other subdetector in STAR detector which would be able to provide information

as TPC, therefore it is not possible to perform any measurements without the TPC. In addition most of other STAR subdetectors use information from the TPC and so are fully dependent on the TPC. All information about the TPC was taken from Ref. [19].

2.2.3 Barrel Electro-Magnetic Calorimeter

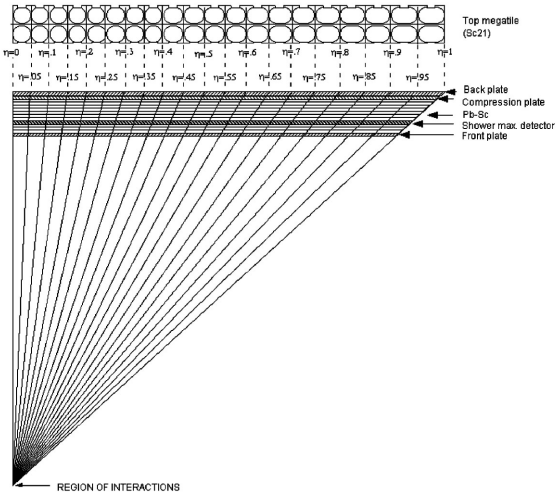

Fig. 2.10: Scheme of BEMC layout. Only half of the longitudinal coverage is shown. Taken from Ref. [20].

The Barrel Electro-Magnetic Calorimeter (BEMC) is detector dedicated primarily for identification of particles with $p_T > 2\,\mathrm{GeV}/c$. It has the same space coverage as the TPC, i.e. full 2π coverage in azimuthal direction and $|\eta| < 1$ in longitudinal direction. The layout of the BEMC is shown in Fig. 2.10. The BEMC consists of 40 modules, inside which there are 20 layers of 5 mm thick lead plates, which serve as an absorber, then there are 21 scintillator layers, which detect the charged showers via set of photomultipliers. A BEMC module is shown in Fig. 2.11.

The particle identification in the BEMC is based on measurement of energy deposited in the calorimeter. To be more specific, quantity $\frac{p}{E}$ is used, where p is particle momentum and E is energy deposited in the BEMC. This ratio is around unity for electrons, as they loose practically all their momentum (energy) in the BEMC. Hadrons (eg. protons), on the other hand, loose just a fraction of their momentum in the BEMC, so the $\frac{p}{E}$ ratio is much bigger than unity.

As can be seen in Fig. 2.10 and Fig. 2.11, there is part of the BEMC called Shower Maximum Detector (SMD). It consists of two perpendicular wire

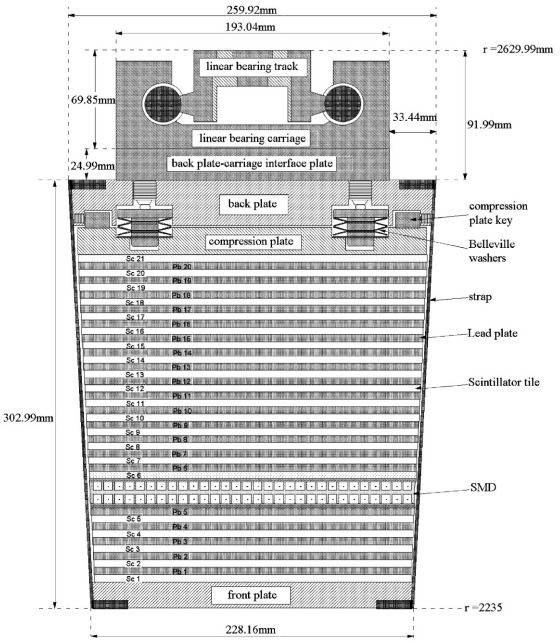

Fig. 2.11: Schematic view of BEMC module. Taken from Ref. [20].

proportional detectors, which provide good spatial resolution of showers created in the BEMC. Simplified scheme of the SMD is in Fig. 2.12.

Generally the BEMC together with the SMD provides good energetic and spatial resolution necessary for efficient particle identification. All information about the BEMC+SMD was taken from Ref. [20].

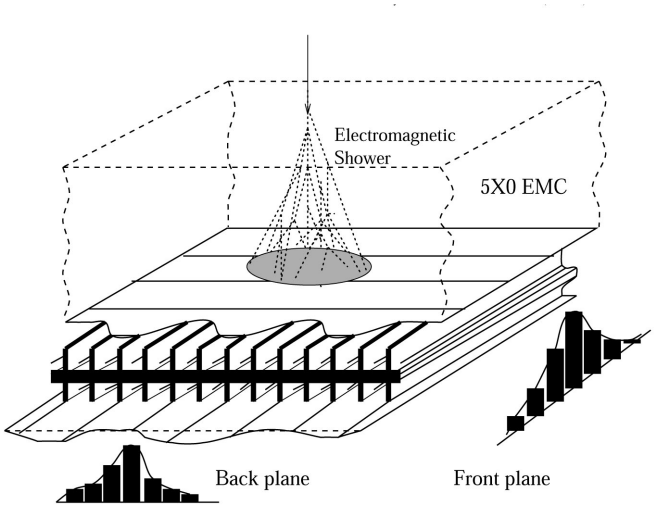

Fig. 2.12: Scheme of STAR BEMC SMD. Taken from Ref. [20].

2.2.4 Time Of Flight system

For low-p_T particle identification ($p_T < 2\,\mathrm{GeV}/c$) the BEMC can not be used. For this purposes the Time Of Flight detector is used. It uses information from the Vertex Position Detector (see Fig. 2.3) and TOF MRPC (Multi-gap Resistive Plate Chambers) shown in Fig. 2.13. More specifically the TOF uses the time difference Δt between signal in the VPD and MRPC. With additional information about particle path-length L from the TPC, the TOF is able to determine the particle speed β according to

$$\frac{1}{\beta} = \frac{c\Delta t}{L}. \tag{2.1}$$

The VPD contains Pb absorber and fast plastic scintillators read out by photomultipliers. The MRPC consists of glass plates with uniform spacing. The gaps between the plates are filled with gas (90% $C_2H_2F_4$, 5% iso-butane, 5% SF_6), which is ionised by passing particles. The created electrons are accelerated in strong electric field, creating avalanches, which are subsequently detected by pads (red in Fig. 2.13).

So that the TOF provides additional information and together with BEMC provides complete information about particle identification.

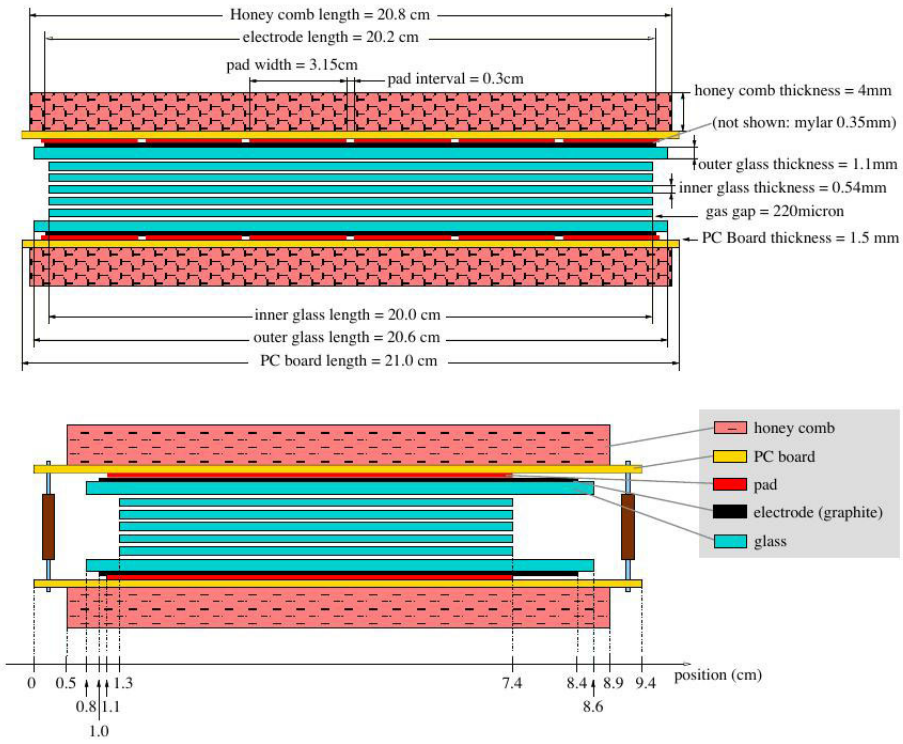

Fig. 2.13: Schematic view of MRPC (Multi-gap Resistive Plate Chamber) used in STAR TOF (Time Of Flight) detector. Taken from Ref. [21].

Chapter 3

Non-photonic electrons

3.1 Motivation for NPE measurement

Non-photonic electrons (NPE) come from semi-leptonic decay of open-heavy flavor mesons, i.e. D mesons containing c quark and B mesons containing b quark. Properties of open heavy-flavor mesons are listed in Tab. 3.1. Heavy quarks are created predominantly in the initial phase of the heavy-ion collisions, during the hard scattering. The QGP fireball is ignited afterwards and the heavy mesons have to pass through it, which consequently provides valuable information about the QGP itself.

Meson	M [GeV/c^2]	$c\tau$ [μm]
D^0 ($c\overline{u}$)	1.865	123
D^+ ($c\bar{d}$)	1.868	312
B^0 ($d\bar{b}$)	5.279	459
B^+ ($u\bar{b}$)	5.279	491

Tab. 3.1: Properties of open-heavy flavor mesons. Shown is their quark composition (left column), mass M (middle column) and mean lifetime τ (right column). Corresponding antiparticles (not shown) have the same properties (M and τ). Taken from Ref. [22].

The open-heavy flavor mesons have too short lifetime to be detected directly, but have to be reconstructed via their decay product. Mainly two decay channels are used in experiments - the hadronic channel, were all products are hadrons (predominantly lighter mesons), or the semi-leptonic channel, where one or more hadrons, together with leptonic pair, are created. The leptonic pair consists of either electron/positron or muon and corresponding neutrino.

When using semi-leptonic channel, only electrons are used, as they are rel-

atively easy to detect and they are created in relatively large number, because the branching ratio of semi-leptonic decays (containing electron/positron, not muons) of open-heavy flavor is approximately 10% [22]. The semi-leptonic channel has also advantage compared to the hadronic one that only one decay product has to be reconstructed, which is sufficient to obtain information about open heavy-flavor production.

On the other hand, reconstructing just NPE does not provide information about mother particle kinematics, e.g. its momentum. In addition, there is relatively large background consisting of gamma conversion electrons, Dalitz decay electrons from π^0 and η mesons and electron-positron pairs from decay of J/ψ. Correct and efficient subtraction of this background is the main challenge in NPE analysis. One way of obtaining the NPE spectrum is to reconstruct the background first and then subtract it from the inclusive electron spectrum. This method is enough, when combined NPE spectrum from D and B mesons decay is required, but it can not provide direct information about D and B mesons separately.

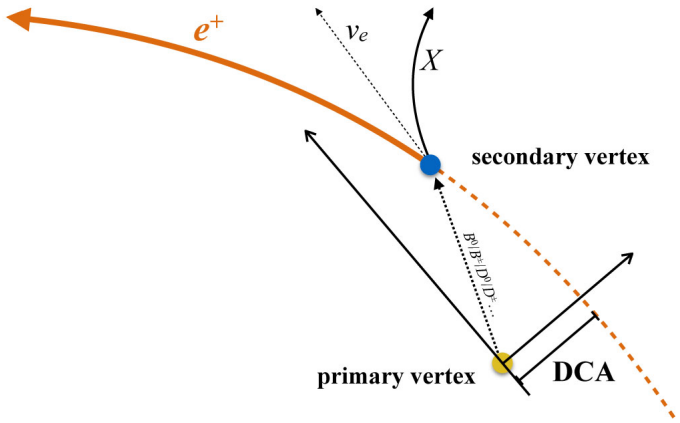

Fig. 3.1: Scheme demonstrating the DCA (distance of closest approach to the primary vertex). Taken from Ref. [16].

For that reason, another method of NPE measurement was developed, which uses the fact that B mesons have significantly longer lifetime and path-length than D mesons (see Tab. 3.1). When a detector with good primary and secondary vertex position resolution is available, it is possible to tell apart B and D mesons by measurement of the distance of closest approach to the primary vertex (denoted DCA, or alternatively d_0), which is shortest distance between the reconstructed primary vertex and track of one of the decay products, in this case electron/positron, in plane transverse to the beam axis, as shown in Fig. 3.1.

3.2 NPE measured at RHIC and LHC

A selection of NPE results is presented in this section. First subsection summarises data measured by ALICE experiment at the LHC, the second one shows results by PHENIX experiment ar the RHIC and the last one takes results obtained by STAR experiment at the RHIC.

3.2.1 ALICE experiment results

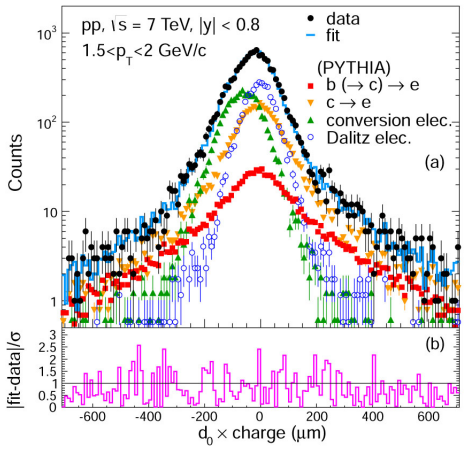

Fig. 3.2: (a) DCA (d_0) distribution measured by ALICE. Black points represent measured inclusive electrons, the other colored points are PYTHIA simulated distributions of individual electron sources (see label in the plot). The blue line is fit of the data and was obtained as sum of the simulated distributions, where the free parameter were the normalisation. (b) Comparison of data and fit. Taken from Ref. [23].

ALICE (A Large Ion Collider Experiment) is experiment at the LHC dedicated primarily to study of heavy-ion (Pb+Pb) collisions, but it also takes reference data from proton-proton collisions and p+Pb collisions. NPE measurement was performed for all of these colliding systems at ALICE where both above described analysis methods were used (background subtraction and DCA).

The DCA method was used for example in Ref. [23] for proton-proton collisions at $\sqrt{s} = 7$ TeV. The basic steps of the analysis are as follows: In first step the inclusive electrons spectrum was obtained. The inclusive electron DCA distribution was than fitted by function containing information about individual contributions to the inclusive electron spectrum. The fit function was obtained from PYTHIA simulation and the normalisation was used and the free parameter of the fit. The DCA distribution, the simulated components and the fit are plotted in Fig. 3.2.

The fit contains information about ratio of the inclusive electron spectrum components which allows to obtain spectrum of required component, in this case NPE from c and b quarks. Spectrum of NPE from decay of D and B mesons is in Fig. 3.3, where comparison with FONLL model is also provided. The obtained result is with good agreement with the model, so the DCA method seems to give correct results.

If the same procedure is applied to different colliding system, it is possible to compare it to the proton-proton result. As an example, measurement of nuclear modification factor R_{pPb} is presented[1]. The R_{pPb} as a function of p_T can be seen in Fig. 3.4. In this case, p+Pb at $\sqrt{s_{NN}} = 5.02\,\text{TeV}$ data was compared to the proton-proton data. This result suggest that there is no significant suppression or enhancement in p+Pb compared to proton-proton system (within errors), i.e. there is no QGP present in p+Pb collisions.

[1]The R_{pPb} compares p+Pb collisions to the proton-proton collisions in the same way as the R_{AA} compares heavy-ion collisions to the proton-proton collisions.

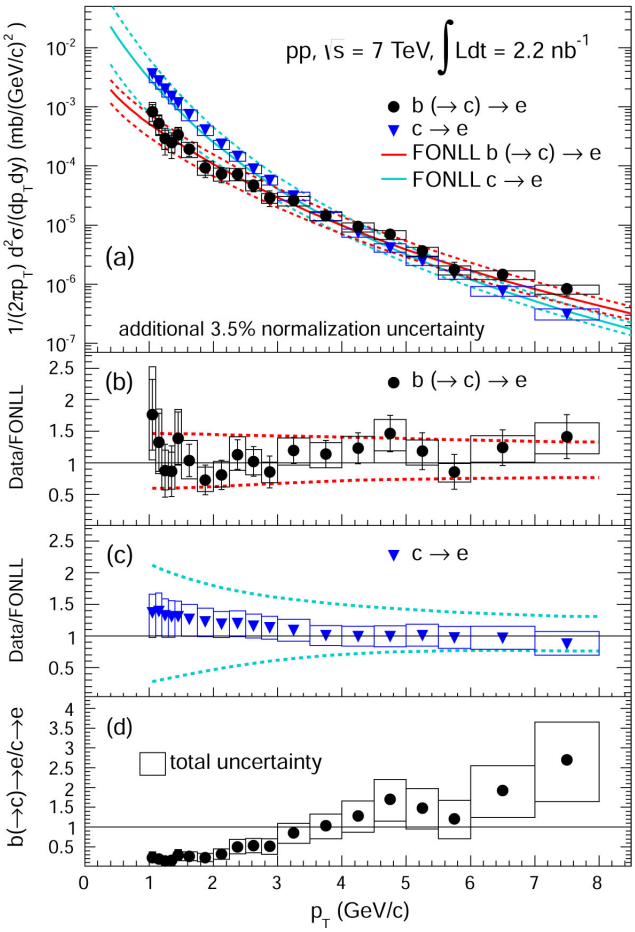

Fig. 3.3: (a) NPE cross-section as a function of p_T for proton-proton collisions at $\sqrt{s} = 7$ TeV measured by ALICE. The black circles represent signal from B mesons decay, the blue triangles represent signal from D mesons decay. The colored lines are prediction by FONLL model. (b) Comparison of data and model for B mesons decay. (c) Comparison of data and model for D mesons decay. (d) Comparison of cross-sections from B mesons and D mesons decay. Taken from Ref. [23].

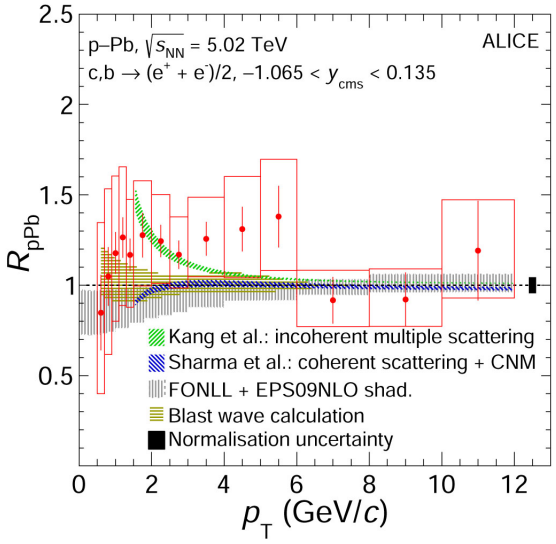

Fig. 3.4: Nuclear modification factor R_{pPb} of NPE as a function of p_T for p+Pb collisions at $\sqrt{s_{NN}} = 5.02$ TeV measured by ALICE. Several models are also plotted for comparison. Taken from Ref. [24].

3.2.2 PHENIX experiment results

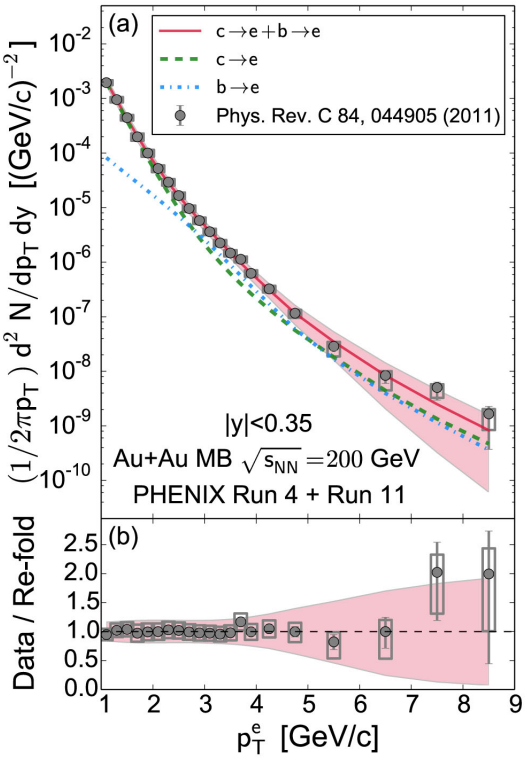

Fig. 3.5: (a) Invariant yield of NPE as a function of p_T for Au+Au collisions at $\sqrt{s_{NN}} = 200$ GeV measured by PHENIX (grey circles, [25]) and re-folded NPE spectra from D and B mesons decay (colored lines). (b) Comparison of data and re-folded spectrum. Taken from Ref. [26].

PHENIX has also performed NPE measurement. As an example an invariant yield of NPE is presented in Fig. 3.5. The grey circles represent PHENIX analysis of data taken in the year 2002, where the NPE spectrum was obtained using the background subtraction method [25]. The colored lines are re-folded NPE spectra from D and B mesons decay [26]. Combination of data from Run4 (year 2004) and Run11 (year 2011) were used for the unfolding. The Run4 data were analysed using background subtraction method, the Run11 data were analysed using the DCA method. As can be seen in panel (b) of Fig. 3.5 the measured and re-folded data are in agreement with each other.

3.2.3 STAR experiment results

STAR experiment does not have any official results of NPE measurement using the DCA, because the old inner silicon detector, the SVT, which was in operation

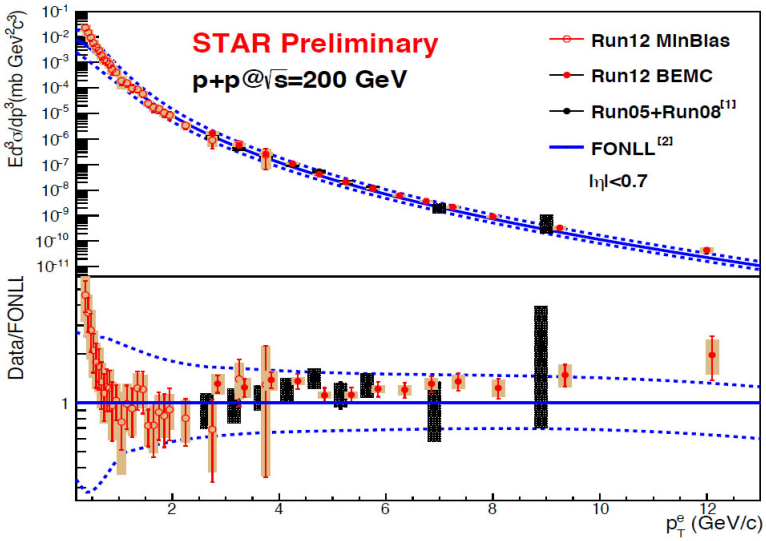

Fig. 3.6: (a) NPE cross-section as a function of p_T for Run12 proton-proton collisions at $\sqrt{s} = 200$ GeV measured by STAR. FONLL model and data from Run05+Run08 [27] are also plotted. (b) Comparison of data and FONLL model. Taken from Ref. [28].

until year 2014, did not have sufficient primary and secondary vertex resolution to tell apart D and B mesons. All presented data are therefore obtained by the photonic background subtraction method.

NPE cross-section as a function of p_T from proton-proton collisions at $\sqrt{s} = 200$ GeV can be seen in Fig. 3.6. In this case the D and B mesons are not distinguished. Comparison to FONLL model is provided in panel (b) of Fig. 3.6, which shows that the measurement is in agreement with the model within uncertainties.

STAR also performed NPE measurement for Au+Au collisions and compared them to the proton-proton collisions. Example of such measurement is shown in Fig. 3.7, where nuclear modification factor R_{AA} as a function of p_T is plotted. Several models are also show in the plot for reference. The suppression observed in central Au+Au collisions is consistent with presence of the QGP. On the other hand, practically no suppression is observed in peripheral Au+Au collisions.

Another interesting NPE measurement is observation of elliptic flow v_2 of open-heavy flavor mesons (NPE) in Au+Au collisions at $\sqrt{s_{NN}} = 200$ GeV, as shown in Fig. 3.8. Method of cumulants was used in the analysis. Comparison with several models is provided and the data is in relatively good agreement with most of the models within errors.

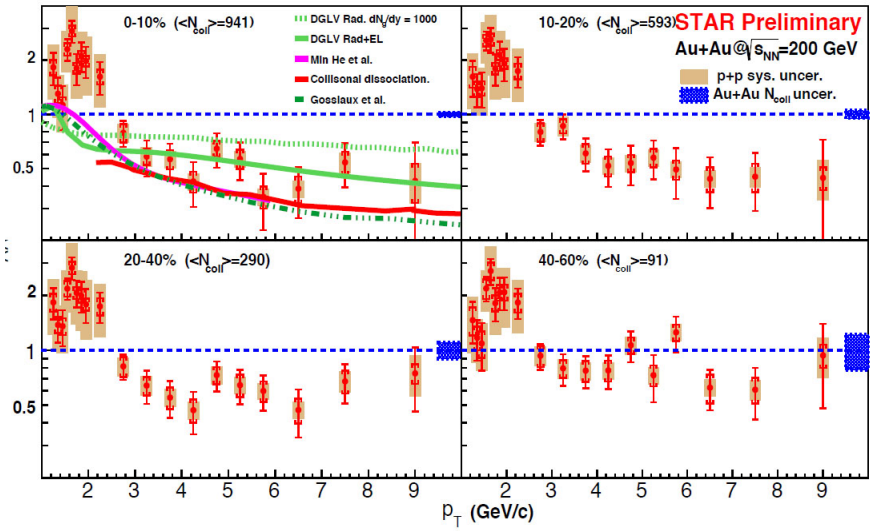

Fig. 3.7: Nuclear modification factor R_{AA} of NPE as a function of p_T for Au+Au collisions at $\sqrt{s_{NN}} = 200$ GeV measured by STAR. Several models are also plotted. Taken from Ref. [28].

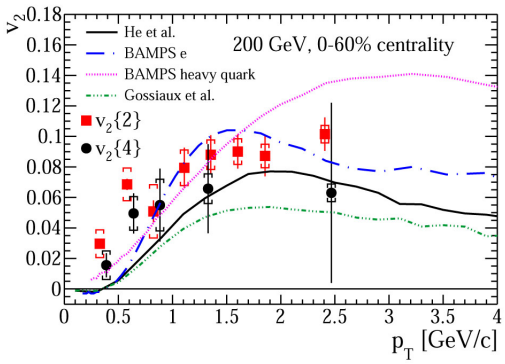

Fig. 3.8: Elliptic flow v_2 of NPE as a function of p_T for Au+Au collisions at $\sqrt{s_{NN}} = 200$ GeV measured by STAR. Method of cumulants was used. Several models are plotted for comparison. Taken from Ref. [29].

Chapter 4

NPE in Au+Au at $\sqrt{s_{NN}} = 200$GeV

4.1 Data and software

Analysis of Au+Au collisions at $\sqrt{s_{NN}} = 200$ GeV is introduced in this chapter. The primary goal of this analysis is to obtain invariant yield NPE spectra from decay of D and B mesons using the DCA method. Run14 (year 2014) data measured by STAR detector were used, more specifically Run14 PicoDst, version P15ic, produced centrally by HF PWG (Heavy-Flavor Physics Working Group). The PicoDst are ROOT-tree-like files generated from STAR MuDst files by applying specific event and/or track quality cuts in order to reduce size of analysed data. The specific cuts used for Run14 P15ic PicoDst can be found in [30]. In addition the PicoDst contain all the necessary information about all accepted tracks from individual subdetecors of the STAR detector.

The code used to analyse the data is based on code written by Kunsu OH from Pusan National University and Mustafa Mustafa from Lawrence Berkeley National Laboratory (LBL). The code was built at NERSC PDSF using STAR library SL15c. The base code is able to extract required information from PicoDst with additional track cuts defined by user. The result are stored in ROOT histograms, also defined by user, to reduce size of the final files compared to ROOT trees.

4.2 Preliminary results

The initial step into the NPE analysis was to get acquainted with the base code and to be able to use it to obtain relevant results in form of histograms. The first attempt was to obtain electron-positron low invariant mass M_{inv} spectrum in order to have information about photonic background to the NPE. Example of such spectrum measured by STAR is shown in Fig. 4.1.

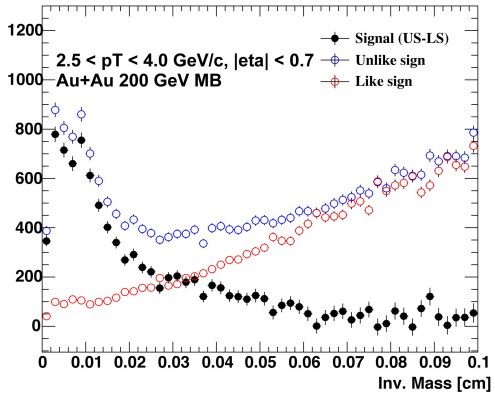

Fig. 4.1: Low invariant mass spectrum of electron-positron pairs measured by STAR in Au+Au collisions at $\sqrt{s_{NN}} = 200$ GeV. Blue points represent unlike-sign pairs, the red are like-sign pairs and the black are the signal (like-sign minus unlike-sign). Taken from Ref. [16].

nTPChitPoints > 20
nTPChitFit > 10
DCA > 1.5 cm
$\|\eta\| < 1.0$ (Fig. 4.2)
$\|\eta\| < 0.7$ (Fig. 4.3)

Tab. 4.1: Additional track quality cuts to the cuts used in PicoDst production.

There are two types of cuts applied in analysis presented in this thesis. The first are additional track quality cuts to the cuts applied in PicoDst production and are listed in Tab. 4.1. The second type of cuts are electron identification cuts, which should provide pure inclusive electrons spectrum, i.e. get rid of hadron contamination. Information from HFT, TPC, TOF and BEMC+SMD was used for "leading" electron, only information from TPC was used for reconstructed partners. Requirement of the HFT in this analysis means at leas one hit in inner layer of the PXL, one hit in outer layer of the PXL and one hit in the IST (i.e. minimum of three hits in three different layers of the HFT). TOF was used for tracks with $p_T < 2$ GeV/c only, BEMC+SMD was used for tracks with $p_T > 2$ GeV/c only. Just tracks with 0.3 GeV/$c < p_T < 5$ GeV/c were accepted. The specific values of electron identification cuts are listed in Tab. 4.2.

The low invariant mass electron-positron pair spectrum obtained in this analysis is shown in Fig. 4.2. This spectrum was obtained by analysing approx. 1M events in 150 PicoDst files. This is therefore relatively small sample, but purpose of this figure was to validate that the code and the cuts are working properly. The final (black stars) and the like sign spectrum (red stars) seems to

$p_T < 2\,\mathrm{GeV}/c$	$p_T > 2\,\mathrm{GeV}/c$
$-1 < n\sigma < 3$	$-1 < n\sigma < 3$
$\left\lvert\frac{1}{\beta} - 1\right\rvert < 0.025$	$0.1c^{-1} < \frac{p}{E} < 2c^{-1}$
	$\lvert \mathrm{d}\phi \rvert < 0.02$ cm
	$\lvert \mathrm{d}z \rvert < 10$ cm
	$\lvert TOWdist \rvert < 0.02$
	BSMD $\lvert\phi\rvert > 1$; $\lvert\eta\rvert > 1$

Tab. 4.2: Electron identification cuts.

be correct, but the unlike-sign spectrum is missing the significant increase for $M_{inv} < 0.2\,\mathrm{GeV}/c^2$ (compare to Fig. 4.1).

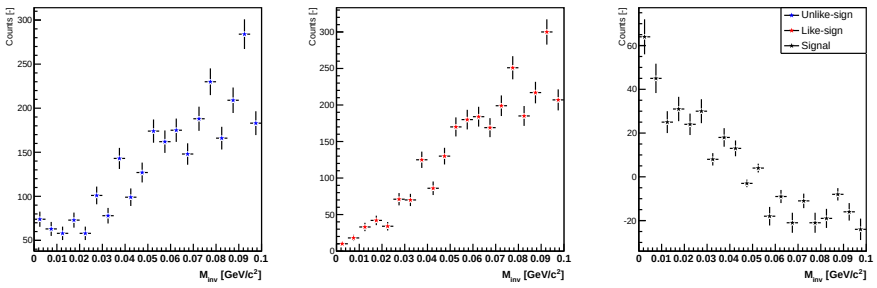

Fig. 4.2: Low invariant mass spectrum of electron-positron pairs measured in Au+Au collisions at $\sqrt{s_{NN}} = 200$ GeV for approx. 1M events. Blue points represent unlike-sign pairs, the red are like-sign pairs and the black are the signal (like-sign minus unlike-sign).

Bigger data sample of approx. 30M events in 5,000 PicoDst files was analysed, which resulted in Fig. 4.3. It is important to note that the η cut was different than in previous case as listed in Tab. 4.1. Even though the statistics is increased compared to the Fig. 4.2, the result is no closer to expected shape of the dependence. The cause of these problems still remains unresolved and it is one of the main goals of further analysis to identify the source of the issues.

For that reason, the same 30M events as before were analysed, but this time without HFT required for the "leading" electron track. The result of this analysis is shown in Fig. 4.4. Compared to Fig. 4.3, the main difference is that there is much more events, which passed the cuts, which is natural, as the cut is not that restrictive this time. The other noticeable thing is that the final spectrum is more smooth than the one in Fig. 4.3, which is most likely caused by increased statistics.

Therefore it can be assumed, that if the statistics is increased even further, the result will be noticeably better. It is therefore planned to run the analysis on sample of approx. 100M events. This should provide sufficient number of

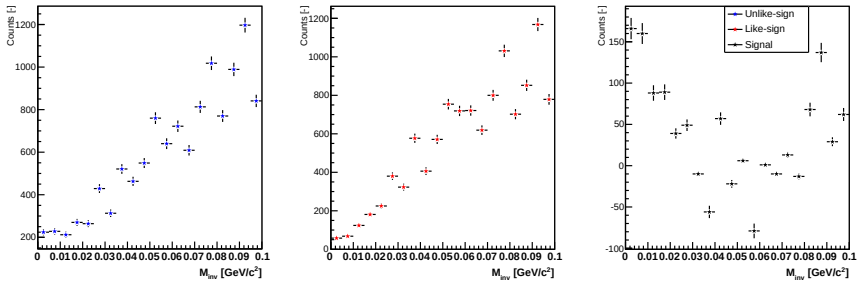

Fig. 4.3: Low invariant mass spectrum of electron-positron pairs measured in Au+Au collisions at $\sqrt{s_{NN}} = 200$ GeV for approx. 30M events. Blue points represent unlike-sign pairs, the red are like-sign pairs and the black are the signal (like-sign minus unlike-sign).

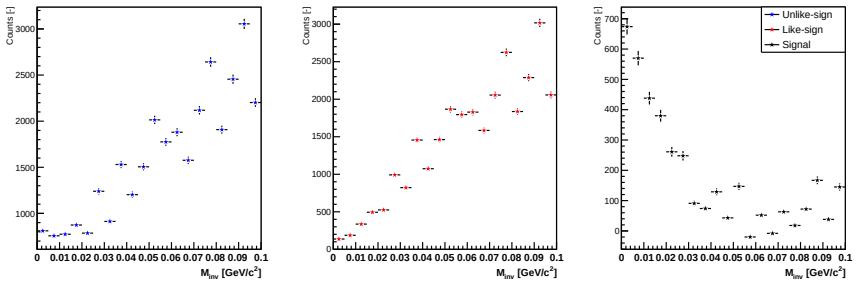

Fig. 4.4: Low invariant mass spectrum of electron-positron pairs measured in Au+Au collisions at $\sqrt{s_{NN}} = 200$GeV for approx. 30M events without HFT required for the "leading" electron track. Blue points represent unlike-sign pairs, the red are like-sign pairs and the black are the signal (like-sign - unlike-sign).

events, which pass the cuts and the plots will be better as a result. Another thing, which will be done, is plotting cuts check histograms to ensure correctness of currently preset cuts.

So to conclude, these results are still very preliminary and have to be considered just as working plots. Cuts will be checked in further analysis by plotting appropriate cuts-check plots and, in addition, the statistics will be increased by analysing at least 100M events.

4.3 Run14 PicoDst data reproduction

It was discovered by the FH PWG, that the HFT efficiency is too low (1/3 of expected value) in Au+Au at $\sqrt{s_{NN}} = 200$ GeV Run14 PicoDst, version P15ic. Fortunately the problem was caused by error during the PicoDst production

and not by the HFT itself. For that reason a reproduction of Run14 Au+Au at $\sqrt{s_{NN}} = 200$ GeV started in April, 2016. The new version is denoted P16id.

New Run14 PicoDst have also updated inner structure. It is therefore necessary to adapt existing NPE analysis code to the new PicoDst standard. This step can not be avoided, as the old, version P15ic, data will be deleted as soon as the reproduction is finished.

Chapter 5

Discussion and conclusion

The analysis of non-photonic electrons in heavy-ion collisions was briefly introduced in this thesis. In the first chapter general properties of the heavy-ion collisions were described, the second chapter was about the STAR detector and the RHIC, the third chapter summarised recent results in NPE analysis from ALICE, PHENIX and STAR experiments and the fourth chapter contained introduction to NPE analysis in Run14 Au+Au collisions at $\sqrt{s_{NN}} = 200\,\mathrm{GeV}$ measured by STAR.

First attempt of this analysis was to reconstruct the photonic electron-positron pair invariant mass spectrum. As already discussed in previous chapter, the resulting plots are not completely consistent with the expectation. The significant increase in the unlike-sign spectrum for $M_{inv} < 0.2\,\mathrm{GeV}/c$, as shown in Fig. 4.1, is not observed in this analysis plots. This might be caused partly by relatively low statistics of current plots and also by cut problem.

For that reason the statistics will be increased from approx. 30M events to 100M events and cuts-check plots will be generated. These two precautions should provide sufficient correction of the results. Further step is to proceed to the NPE analysis itself, i.e. to obtain D and B mesons spectrum, using the DCA method.

Existing code will be also adapted to the new PicoDst version, P16id, of the Run14 Au+Au at $\sqrt{s_{NN}} = 200\,\mathrm{GeV}$ data production. The reproduction is necessary as it was discovered that there is an HFT efficiency problem in older PicoDst version, P15ic, of this dataset. Newly produced PicoDst should improve the statistics as the HFT efficiency should be three times better in new production than in the old one.

Bibliography

[1] M. Kliemant et al., Global Properties of Nucleus-Nucleus Collisions, Lect.Notes Phys.785:23-103,2010.

[2] K. Yagi et al., Quark-gluon Plasma, Cambridge University Press 2005.

[3] STAR collaboration, et al., Energy Dependence of Moments of Net-proton Multiplicity Distributions at RHIC, Phys. Rev. Lett. 112 (2014) 032302.

[4] T. Hirano et al., Hydrodynamics and flow, 2008, arXiv:0808.2684v1 [nucl-th].

[5] B. Müller, Investigation of hot QCD matter: Theoretical aspect, 2013, arXiv:1309.7616v2 [nucl-th].

[6] S. Chatrchyan, et al., Study of high-p_T charged particle suppression in PbPb compared to pp collisions at $\sqrt{s_{NN}} = 2.76$ TeV, Eur. Phys. J. C 72 (2012) 1945.

[7] S. Voloshin and Y. Zhang, Flow study in relativistic nuclear collisions by Fourier expansion of Azimuthal particle distributions, Z.Phys. C70 (1996) 665-672.

[8] G. Aad, et al., Measurement of the azimuthal anisotropy for charged particle production in $\sqrt{s_{NN}} = 2,76$ TeV lead-lead collisions with the ATLAS detector, Phys. Rev. C 86 (2012) 014907.

[9] B. Abelev, et al., Elliptic flow of identified hadrons in Pb–Pb collisions at $\sqrt{s_{NN}} = 2,76$ TeV, CERN-PH-EP-2014-104.

[10] D. d'Enteria, B. Betz, High-p_T hadron suppression and jet quenching, Lect.Notes Phys.785:285-339, Springer 2010.

[11] STAR collaboration, Evidence from d+Au measurements for final-state suppression of high pT hadrons in Au+Au collisions at RHIC, Phys. Rev. Lett. 91 (2003) 072304.

[12] G. Roland, et al., Heavy-ion collisions at the LHC, Prog.Part.Nucl.Phys. 77 (2014) 70-127.

[13] BLN official website, `https://www.bnl.gov/rhic/linac.asp`, visited 21st June 2016.

[14] M. Harrison, et al., RHIC project overviwe, Nuclear Instruments and Methods in Physics Research A 499 (2003) 235–244.

[15] J. G. Alessi, et al, The Brookhaven National Laboratory electron beam ion source for RHIC, The Review of scientific instruments 81(2):02A509, February 2010

[16] K. OH, Measurements of Charm and Bottom Productions in Semi-leptonic Channels at STAR, Poster, Quark Matter 2015 (Kobe, Japan).

[17] K. H. Axkermann, et al., STAR detector overview, Nuclear Instruments and Methods in Physics Research A 499 (2003) 624–632.

[18] D. Beavis, et al., The STAR Heavy Flavor Tracker, Technical Design Report, March 15, 2011.

[19] M. Anderson, et al., The STAR Time Projection Chamber: A Unique Tool for Studying High Multiplicity Events at RHIC, Nuclear Instruments and Methods in Physics Research A 499 (2003) 659–678.

[20] M. Beddo, et al., The STAR Barrel Electromagnetic Calorimeter, Nuclear Instruments and Methods in Physics Research A 499 (2003) 725–739.

[21] STAR TOF collaboration, Proposal for a Large Area Time of Flight System for STAR, May 24, 2004.

[22] K. A. Olive, et al., Review of Particle Physics, Chin. Phys. C, 38, 090001 (2014).

[23] ALICE collaboration, Measurement of electrons from beauty hadron decays in pp collisions at $\sqrt{s} = 7$ TeV, CERN-PH-EP-2012-229.

[24] ALICE collaboration, Measurement of electrons from heavy-flavour hadron decays in p-Pb collisions at $\sqrt{s_{NN}} = 5.02$ TeV, Phys. Lett. B 754 (2016) 81-93.

[25] PHENIX collaboration, Heavy Quark Production in p+p and Energy Loss and Flow of Heavy Quarks in Au+Au Collisions at $\sqrt{s_{NN}} = 200$ GeV, Phys. Rev. C 84, 044905 (2011).

[26] PHENIX collaboration, Single electron yields from semileptonic charm and bottom hadron decays in Au+Au collisions at $\sqrt{s_{NN}} = 200$GeV, Phys.Rev. C93 (2016) no.3, 034904

[27] STAR collaboration, High p_T non-photonic electron production in $p + p$ collisions at $\sqrt{s_{NN}} = 200$ GeV, Phys. Rev. D 83 (2011) 52006.

[28] X. Bai, Measurements of electrons from semileptonic decays of open heavy flavor hadrons in p+p and Au+Au collisions at $\sqrt{s_{NN}} = 200$ GeV, Poster, Quark Matter 2015 (Kobe, Japan).

[29] STAR collaboration, Elliptic flow of non-photonic electrons in Au+Au collisions at $\sqrt{s_{NN}} = 200$, 62.4 and 39 GeV, arXiv:1603.05477v3 [nucl-ex]

[30] LBL Soft Physics Group PicoDst website, `http://rnc.lbl.gov/~xdong/SoftHadron/picoDst.html`, visited 9th June 2016.